

Ex-Solved Ag Nanocatalysts on a Sr-Free Parent Scaffold Authorize a Highly Efficient Route of Oxygen Reduction

Jun Hyuk Kim, Jun Kyu Kim, Han Gil Seo, Dae-Kwang Lim, Seung Jin Jeong, Jongsu Seo, Jinwook Kim, and WooChul Jung*

The electrocatalytic value of nanoparticles has attracted substantial attention in relation to energy conversion devices, including solid oxide fuel cells. Among various forms of analogs, ex-solved metal nanoparticles originating from their parent oxides display strong particle-substrate interactions and thus have the benefits of extended durability and of course enhanced catalytic activity. Inspired by recent advances, here, novel air-electrode materials based on $\text{BaCoO}_{3-\delta}$ perovskites decorated with socketed Ag nanoparticles are presented. Doping with niobium (Nb^{5+}) and tantalum (Ta^{5+}) can significantly promote the stability of the cubic perovskite phase. The developed oxides exhibit promising performance outcomes in the highly prized low-to-intermediate temperature regimes (450–650 °C). Moreover, the exclusion of Ag particles further activates the parent scaffold, thereby conveying record-level area-specific resistance (e.g., $\approx 0.02 \Omega \text{ cm}^2$ at 650 °C). Coupled with the unique nanoarchitecture, the newly designed cathode showcases in this study hold great promise for future air-electrodes in fuel cells.

resistance;^[2,4] prevented coarsening and/or coalescence between particles even at elevated temperatures;^[2] and successfully leveraged H_2 electro-oxidation,^[5,6] CO_2 electrolysis,^[7,8] CO oxidation,^[6,9] and steam reforming,^[4] among other processes.

Given that the ex-solution process utilizes the oxygen chemical potential as a driving force to drag “catalytic gems” out of the crystal lattice,^[9] annealing at reducing atmospheres is often done to nucleate and ripen the metal nanoparticles.^[8,10] However, the aforementioned treatment limits the applicability of the ex-solution strategy to air-electrode materials, especially those with Co, the structure of which is vulnerable under a reducing atmosphere.^[11] Although most state-of-the-art air-electrodes are based on cobaltite,^[12–15] as commonly illustrated with oxygen nonstoichiometry diagrams,


1. Introduction

The electrocatalytic value of nanoparticles at the surface is of significance in energy conversion devices because the overall performance of these devices is governed primarily by the top-most layer of electrodes.^[1] In a similar vein, less than a decade ago, the “ex-solution” phenomenon fascinated many scientists and engineers given the elegant geometries between metal nanoparticles and oxides.^[2,3] Since then, striking results have been demonstrated in the field of solid oxide electrochemical cells (SOCs) using the ex-solution process as a self-emergent platform, particularly focused on fuel-electrodes. The strong substrate-particle interaction displayed enhanced coking

perovskites with Co as a main constituent readily lose oxygen, causing the structure to decompose or even degrade completely during the reduction step.^[16] Hence, it is necessary to explore the delicate point at which the parent oxide experiences minimal impact but still sufficiently engenders to form metal nanoparticles. To address this challenge, Zhu et al. successfully utilized H_2 -temperature-programmed reduction (TPR) to describe the range of Ag ex-solution temperatures from A-site deficient $\text{Sr}_{0.95}\text{Nb}_{0.1}\text{Co}_{0.9}\text{O}_{3-\delta}$.^[15] Two distinct sets of H_2 -TPR profiles between Ag-doped and undoped perovskites clearly depict the safe temperature window in which to produce Ag nanoparticles with fewer effects on the parent oxide.

With regard to $\text{Sr}_{0.95}\text{Nb}_{0.1}\text{Co}_{0.9}\text{O}_{3-\delta}$, it has become clear lately that $\text{SrCoO}_{3-\delta}$ (SCO)-based perovskites are promising candidates in low-temperature solid oxide fuel cell (SOFC) air-electrodes.^[17] Such perovskites deliver decent oxygen reduction reaction (ORR) performance even in the low-temperature regimes (450–550 °C), where the surface oxygen exchange kinetics can be extremely sluggish. One of the common problems encountered with SCO-based materials, however, is their intrinsic instability and tendency to form brownmillerite ($\text{SrCoO}_{2.5}$) with a hexagonally ordered structure, which exhibits slowness with regard to oxygen electroreduction.^[18] To stabilize the structure, multivalent dopants have been introduced to replace B-site Co ions partially. The doping of Sc,^[19] Nb,^[20] Ta,^[21] Sb,^[22] P,^[23] and Mo^[24] elements represents a successful case of curtailing extravagant vacancies. The co-substitution of two differently

Dr. J. H. Kim, J. K. Kim, Dr. H. G. Seo,^[†] Dr. D.-K. Lim, S. J. Jeong, J. Seo, J. Kim, Prof. W. Jung
Department of Materials Science and Engineering
Korea Advanced Institute of Science and Technology
291 Daehak-ro, Yuseong-gu, Daejeon 34141, Republic of Korea
E-mail: wcjung@kaist.ac.kr

 The ORCID identification number(s) for the author(s) of this article can be found under <https://doi.org/10.1002/adfm.202001326>.

^[†]Present address: Department of Materials Science and Engineering, Massachusetts Institute of Technology (MIT), 77 Massachusetts Avenue, Cambridge, MA, 02139, USA

DOI: 10.1002/adfm.202001326

charged atoms such as SrSc_{0.175}Nb_{0.025}Co_{0.8}O_{3-δ} ($\approx 0.32 \Omega \text{ cm}^2$ at 500 °C)^[25] or SrCo_{0.8}Nb_{0.1}Ta_{0.1}O_{3-δ} ($\approx 0.16 \Omega \text{ cm}^2$ at 500 °C) has also demonstrated superior performance outcomes.^[26] Likewise, the vast majority of studies have concentrated on SCO-based perovskites, whereas the aforementioned doping strategies can be directly utilized with BaCoO_{3-δ} (BCO) perovskites as well.

According to the literature,^[27] the larger ionic radius of the Ba ion can be advantageous for oxygen migration in the lattice. Indeed, it has been reported that the formation of the BCO nanostructure on the surface greatly boosts the rate of the surface oxygen exchange on layered-perovskite cathodes by accelerating the oxygen adsorption and dissociation processes.^[13,28] Moreover, it should be noted that the substitution of Sr²⁺ into Ba²⁺ raises the overall phase stability of cubic perovskites.^[29] In light of the above, BCO perovskites may hold great potential to be the next generation of SOFC cathodes. However, to the best of our knowledge, few studies have deployed cation-substituted BCO perovskites as a solitary backbone to catalyze oxygen. Perhaps this would be a suitable moment to revisit the value of the BCO perovskites.

Inspired by above insights, we report novel cathode materials based on BCO created by integrating an effective doping strategy with the ex-solution concept. Herein, we present the ORR activity of a highly efficient Nb and Ta codoped perovskite, BaCo_{0.8}Nb_{0.1}Ta_{0.1}O_{3-δ} (BCNT), and provide the results of a performance comparison with individually doped samples. We also replaced a small portion of Ba ions with Ag atoms (Ba_{0.95}Ag_{0.05}Co_{0.8}Nb_{0.1}Ta_{0.1}O_{3-δ}, BACNT) for subsequent blueprinting of the ex-solution of nanoparticles (e-BACNT). The ex-solution of Ag nanoparticles remarkably facilitates the oxygen surface exchange rate, thereby resulting in outstanding area-specific resistance (e-BACNT: $\approx 0.02 \Omega \text{ cm}^2$ at 650 °C in a symmetrical cell configuration). The unique multidoping strategy employed in this study can garner immediate interest with regard to the creation of advanced air-electrodes for fuel cells and can be expected to facilitate investigations of materials based on BCO.

2. Results and Discussion

2.1. Physical Characterization of Doped BaCoO_{3-δ}

Three types of isostructural BCO perovskites are synthesized by doping pentavalent ions, in this case niobium (Nb⁵⁺) and/or tantalum (Ta⁵⁺). X-ray diffraction (XRD) reveals that BaCo_{0.9}Nb_{0.1}O_{3-δ} (BCN), BaCo_{0.9}Ta_{0.1}O_{3-δ} (BCT), and BaCo_{0.8}Nb_{0.1}Ta_{0.1}O_{3-δ} (BCNT) share a major cubic perovskite structure with the *Pm-3m* space-group, with a minor lattice constant difference (Figure 1a): BCN ($a = 4.07 \text{ \AA}$), BCT ($a = 4.08 \text{ \AA}$), and BCNT ($a = 4.07 \text{ \AA}$). The cubic structure is further confirmed with Raman spectroscopy (Figure S1a, Supporting Information). The series of developed perovskites displays no observable bands in the Raman spectra, signifying that they have Raman-inactive cubic symmetry.^[14,30]

To qualify as a promising candidate for SOFC cathodes, multiple properties are required, including electronic and/or ionic conductivity, surface oxygen exchange rate, and chemical and structural stability, among others, often making it difficult for single-phase cathodes to satisfy aforementioned characters at once. From this perspective, multiple reports have suggested

that electrodes with a heterostructure can be advantageous as they may meet the aforementioned requirements and allow a dramatically extended triple-phase boundary, which is proven to be pivotal in relation to the ORR.^[13,28,31] Herein, we blueprint the chemical ex-solution of Ag to realize a highly efficient multi-phase electrode. Ag is renowned for its good electronic conductivity coupled with prominent ORR catalytic activity.^[15,32] The low price of Ag, although classified as precious metal, is a bonus. However, the abysmal thermal instability of Ag places it in a dubious position when employing it as high-temperature catalysts. This dilemma can be resolved by applying the ex-solution technique. Unlike physical deposition/mixing, ex-solved metal analogs enjoy exceptional robustness, as nanoparticles are socketed into the parent oxide, thereby protecting metal nanoparticles physically and preventing coarsening and coalescence. In this way, the synergistic effects between Ag particles and perovskite oxides can be anticipated more reliably.

Considering the ionic radii and the oxidation state of Ag⁺ (115 pm), Ag is likely to fit into the A-site with Ba²⁺ (149 pm) rather than into the B-site (Co³⁺: 75 pm, Nb⁵⁺: 64 pm, Ta⁵⁺: 75 pm).^[33] Moreover, Ag is well known to form a perovskite with Nb or Ta, such as AgNbO₃ or AgTaO₃.^[34] Therefore, to accommodate Ag in the perovskite crystal lattice, 5% of the A-site Ba is replaced with Ag, and the modified compositions are as follows: Ba_{0.95}Ag_{0.05}Co_{0.9}Nb_{0.1}O_{3-δ} (BACN), Ba_{0.95}Ag_{0.05}Co_{0.9}Ta_{0.1}O_{3-δ} (BACT), and Ba_{0.95}Ag_{0.05}Co_{0.8}Nb_{0.1}Ta_{0.1}O_{3-δ} (BACNT). Again, XRD discovers no primary change in the cubic perovskite structure (BACN ($a = 4.07 \text{ \AA}$), BACT ($a = 4.07 \text{ \AA}$), and BACNT ($a = 4.07 \text{ \AA}$), implying that Ag is well doped into the BCO perovskites without causing deleterious effects (Figure 1a). Besides, the binding energies of Nb 3d and Ta 4f in the series of BCO perovskites are analyzed with X-ray photoelectron spectroscopy, and it appears that the dopants are in +5 oxidation valence (Figure S2, Supporting Information).

Thereafter, Ag ex-solution takes place by treating the Ag-doped perovskites in a quartz tube under flowing 4% H₂/Ar at 300 °C for 2 h. The ex-solution temperature is assessed using H₂-temperature-programmed reduction (H₂-TPR) (Figure S3, Supporting Information). The H₂-TPR profiles indicate that the Ag-doped perovskites show a discernible reduction peak around $\approx 300 \text{ °C}$.^[15] After a reduction treatment at 300 °C, powder XRD is again conducted (Figure 1b). The lattice constants of the Ag ex-solved perovskites (hereafter e-perovskite oxides) show slight increases (e-BACN ($a = 4.08 \text{ \AA}$), e-BACT ($a = 4.08 \text{ \AA}$), and e-BACNT ($a = 4.09 \text{ \AA}$)); however, all managed to maintain their cubic perovskite structures (Figure S1b, Supporting Information). To compare the effects of the reduction temperature, another set of powder samples is treated at 500 °C (4% H₂/Ar for 2 h). The resulting XRD outcomes show the complete disruption of the perovskite phases (Figure S4, Supporting Information); hence, to avoid any possible damage to the parent oxide, the reduction temperature is set to the minimum level (300 °C).

The morphology and composition of the Ag ex-solved BCO perovskite is investigated with high-resolution transmission electron microscopy (HRTEM) and high-angle annular dark field scanning transmission electron microscope (HAADF-STEM), and the presence of a firmly anchored Ag nanoparticle is confirmed, as shown in Figure 1c,d. Moreover, scanning electron microscopy (SEM) images illustrate well-dispersed

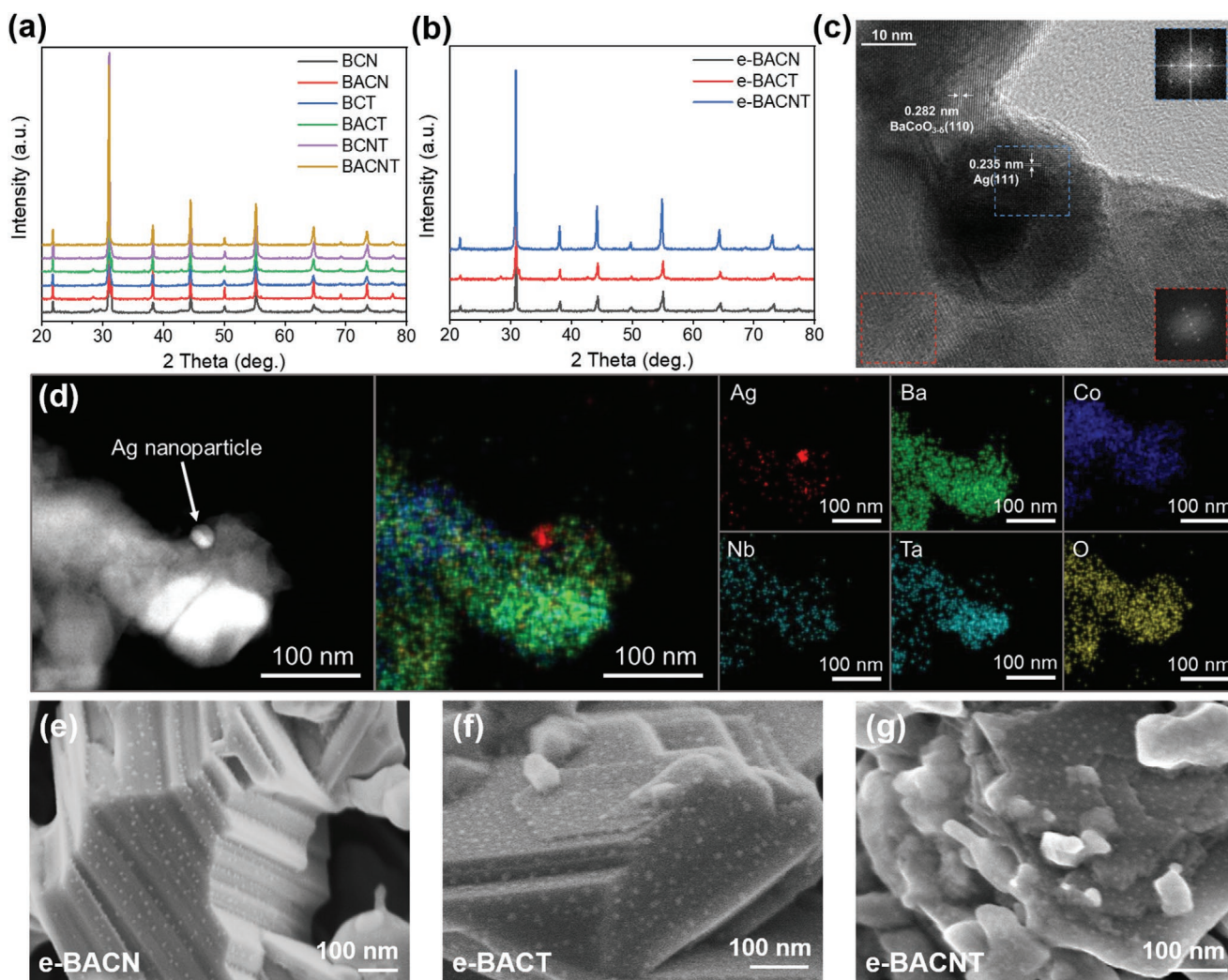


Figure 1. Physical characterization of the doped $\text{BaCoO}_{3-\delta}$: XRD data of the a) as-synthesized cathode materials, and b) powders after the ex-solution process (4% H_2/Ar at 300 °C for 2 h), c) HRTEM image of ex-solved Ag nanoparticles from the $\text{BaCoO}_{3-\delta}$ parent oxide, (inset) fast Fourier transform patterns obtained from the $\text{BaCoO}_{3-\delta}$ host oxide (red box), Ag (blue box), d) HAADF-STEM image of Ag ex-solved $\text{Ba}_{0.95}\text{Ag}_{0.05}\text{Co}_{0.8}\text{Nb}_{0.1}\text{Ta}_{0.1}\text{O}_{3-\delta}$ (e-BACNT) and the corresponding energy-dispersive X-ray spectroscopy (EDX) results, SEM images of the cathode microstructures: e) Ag ex-solved $\text{Ba}_{0.95}\text{Ag}_{0.05}\text{Co}_{0.9}\text{Nb}_{0.1}\text{O}_{3-\delta}$ (e-BACN), f) Ag ex-solved $\text{Ba}_{0.95}\text{Ag}_{0.05}\text{Co}_{0.9}\text{Ta}_{0.1}\text{O}_{3-\delta}$ (e-BACT), and g) e-BACNT.

Ag nanoparticles on the surfaces of porous cathodes after the H_2 -reduction process (Figure 1e–g; please see Figure S5 (Supporting Information) for a comparison between the as-synthesized cathode powder surfaces). Therefore, according to the above analysis, it can be concluded that the ex-solution of Ag was conducted properly here.

2.2. Electrochemical Performance Evaluation of the Doped $\text{BaCoO}_{3-\delta}$

The ORR catalytic activity for the e-BACN, e-BACT, and e-BACNT cathodes are characterized with electrochemical impedance spectroscopy (EIS) in a symmetric cell configuration (Figure 2). Complete sets of the impedance spectra of all developed cathode materials at different temperatures and at different oxygen partial pressures ($p\text{O}_2$), and the corresponding Arrhenius plots along with the activation energies can be found

in Figures S6–S14 (Supporting Information). A Nyquist plot of the impedance spectra shows a depressed arc, attributed to the electrode polarization resistance (R_p). It should also be noted that Ta-doped perovskites outperformed the Nb-doped ones. This can be ascribed to the low electronegativity of Ta as compared to that of Nb, which causes a high level of oxygen deficiency in perovskites.^[26] When Nb and Ta were codoped into BCO perovskites (BCNT), the most prominent performance results were seen, plausibly due to the synergic effects between Nb and Ta (Figure S15, Supporting Information). Nonetheless, the application of the Ag ex-solution dramatically improves the ORR activity of Nb/Ta-stabilized BCO perovskites, therefore reflecting the smaller arc size. Taking e-BACN as an example, the R_p values are only ≈ 0.023 , 0.049, and 0.112 $\Omega \text{ cm}^2$ at 650, 600, and 550 °C, respectively, surpassing the values measured with BACN cathodes (0.07, 0.132, and 0.266 $\Omega \text{ cm}^2$ at 650, 600, and 550 °C). Moreover, the e-BACN electrode, e-BACT, as well as the e-BACNT cathodes undergo enhanced ORR catalytic

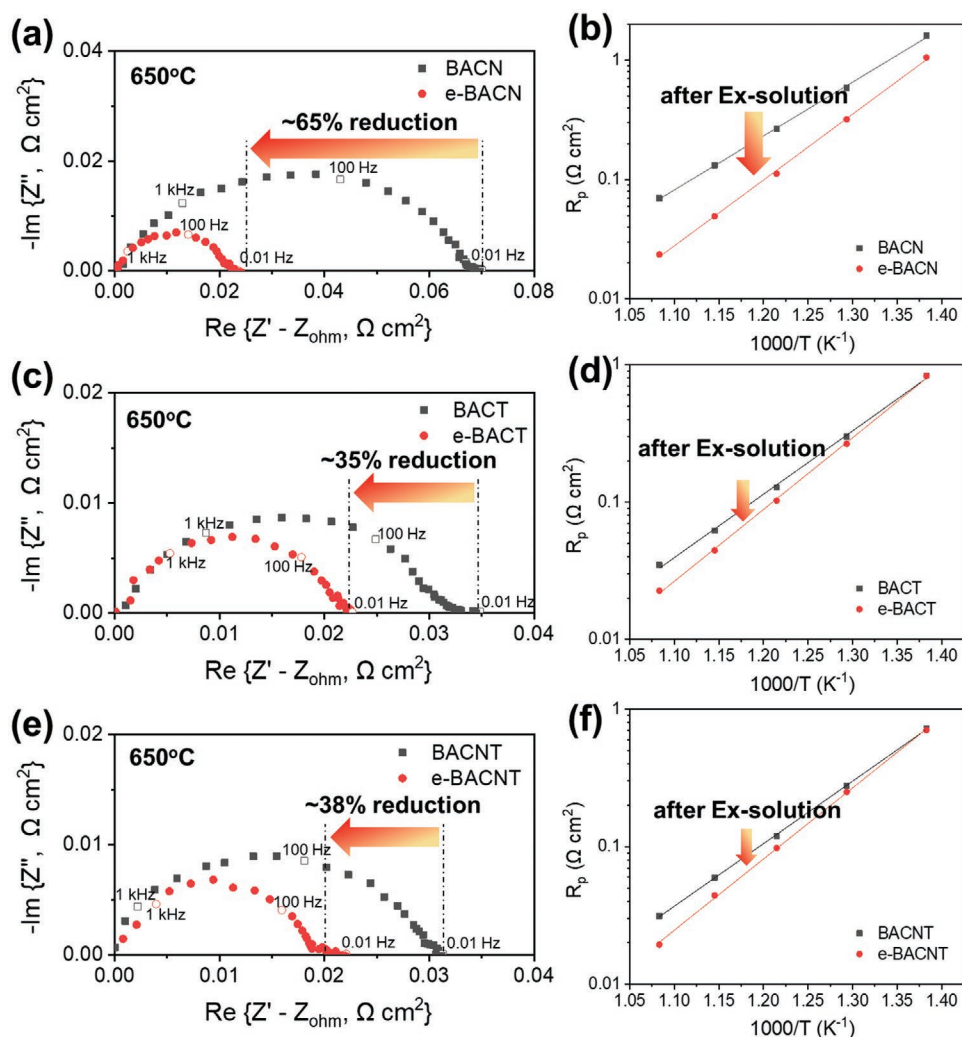


Figure 2. Electrochemical performance evaluation: EIS profiles of a) $\text{Ba}_{0.95}\text{Ag}_{0.05}\text{Co}_{0.9}\text{Nb}_{0.1}\text{O}_{3-\delta}$ (BACN) and Ag ex-solved $\text{Ba}_{0.95}\text{Ag}_{0.05}\text{Co}_{0.9}\text{Nb}_{0.1}\text{O}_{3-\delta}$ (e-BACN), c) $\text{Ba}_{0.95}\text{Ag}_{0.05}\text{Co}_{0.9}\text{Ta}_{0.1}\text{O}_{3-\delta}$ (BACT) and Ag ex-solved $\text{Ba}_{0.95}\text{Ag}_{0.05}\text{Co}_{0.9}\text{Ta}_{0.1}\text{O}_{3-\delta}$ (e-BACT), and e) $\text{Ba}_{0.95}\text{Ag}_{0.05}\text{Co}_{0.8}\text{Nb}_{0.1}\text{Ta}_{0.1}\text{O}_{3-\delta}$ (BACNT) and Ag ex-solved $\text{Ba}_{0.95}\text{Ag}_{0.05}\text{Co}_{0.8}\text{Nb}_{0.1}\text{Ta}_{0.1}\text{O}_{3-\delta}$ (e-BACNT) in symmetric cell configurations (electrode|Sm-doped $\text{CeO}_{2-\delta}$ (SDC, 20% Sm)|electrode). Corresponding Arrhenius plots of the polarization curves are presented in b,d,f).

activity. Therefore, at 650 °C, the electrode performance is promoted by $\approx 35\text{--}65\%$ after the ex-solution of Ag.

To determine the mechanism of ORR promotion when using ex-solved Ag nanocatalysts (Figure 3a), a distribution of relaxation time (DRT) analysis of EIS is performed. With regard to the electrochemical polarization losses of the cathodes, multiple rate-limiting steps are involved to represent one depressed arc in impedance spectroscopy. While the detailed processes of ORR remain elusive in a single arc, a DRT analysis is a powerful tool capable of isolating the complex ORR processes into discrete steps based on the electrochemical circuits with different time constants.^[35] Because the e-BACNT cathodes showed the best performance among various types of Nb/Ta-stabilized BCO perovskites, interpretations of the DRT functions as devised here focus on the e-BACNT cathode as a representative cathode (Figure 3b–e). As shown in Figure 3b, the DRT plots of the e-BACNT cathode show three distinct peaks: the high-frequency (HF), mid-frequency (MF), and low-frequency (LF)

peaks. Each peak addresses a non-identical electrochemical process; Chen et al. suggested that HF is attributed to the charge transfer across the interface, MF is associated with the oxygen surface exchange, and LF is related to the mass transfer processes, such as that by gas diffusion.^[14,28] (Hereafter, the interpretation of DRT mainly relies on these references.)

As shown in Figure 3c, a primary change occurs with the HF peak after the ex-solution process, coupled with a secondary enhancement in the MF peak. This is a strong indicator that Ag nanoparticles greatly bolster the charge transfer process, along with the oxygen surface exchange. The HF+MF enhancements after Ag ex-solution are duplicated in the e-BACN and e-BACT cathodes as well (Figure S16, Supporting Information). When lowering the temperature (Figure 3c), the MF peak becomes more pronounced compared to the HF peak, suggesting that the rate-determining step of the ORR shifts from the charge transfer to the oxygen surface exchange. On the other hand, the LF peak experiences a negligible thermal effect, suggesting

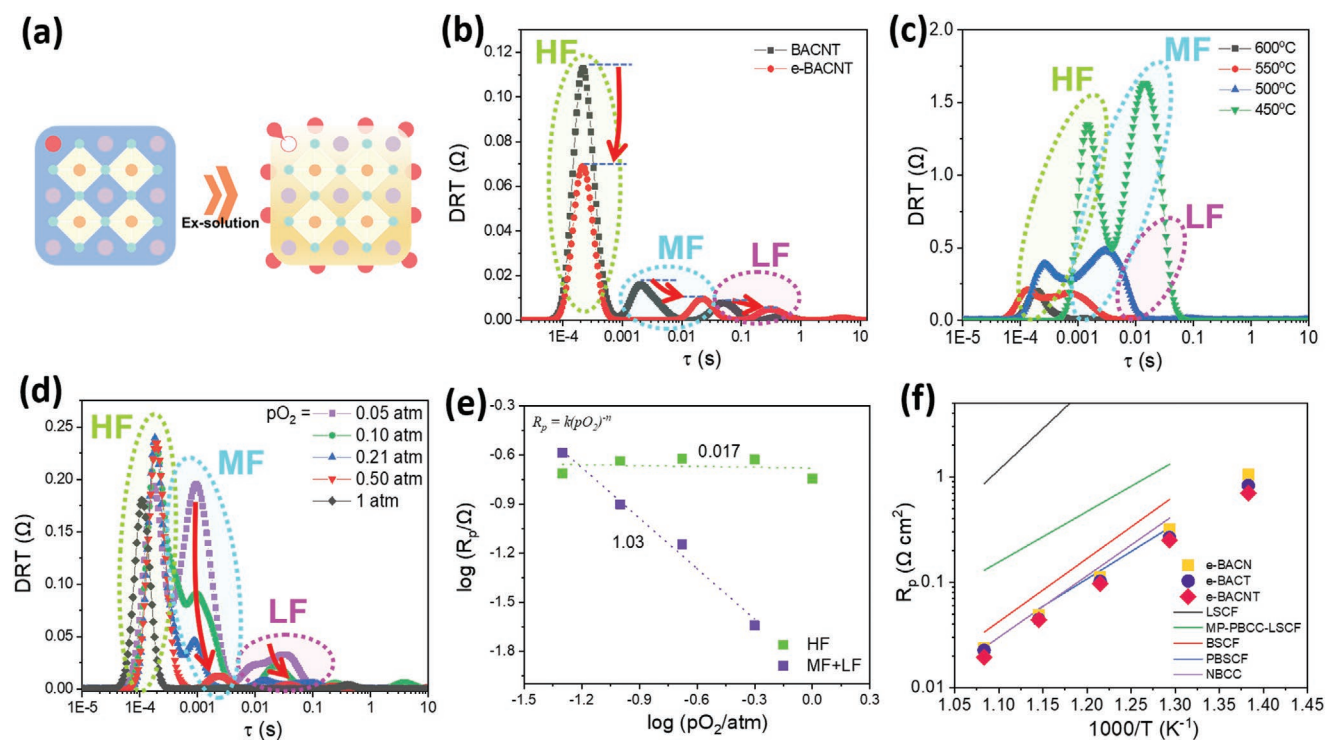


Figure 3. Analysis of the oxygen reduction reaction pathways: a) Schematics of the ex-solution process. b) Distribution of relaxation time (DRT) analyses of porous $\text{Ba}_{0.95}\text{Ag}_{0.05}\text{Co}_{0.8}\text{Nb}_{0.1}\text{Ta}_{0.1}\text{O}_{3-\delta}$ (BACNT) and Ag ex-solved $\text{Ba}_{0.95}\text{Ag}_{0.05}\text{Co}_{0.8}\text{Nb}_{0.1}\text{Ta}_{0.1}\text{O}_{3-\delta}$ (e-BACNT) electrodes. c) Temperature dependence on the DRT functions of e-BACNT. d) Impacts of the oxygen partial pressure on the DRT functions of e-BACNT at 600 °C and e) the corresponding oxygen partial pressure dependency outcomes of HF and MF+LF. f) Mapping of the ORR performance of the developed cathodes over several benchmark materials.^[12,28,37,38a]

that the LF peak is responsible for gas diffusion given that it is less sensitive to temperature variances.^[36] With different levels of $p\text{O}_2$ (Figure 3d), the MF peak is again greatly affected, suggesting that they are closely linked to the processes of oxygen adsorption/desorption, dissociation, and surface transport. If we separate the HF from MF+LF (Figure 3e), the HF displays independent behavior toward $p\text{O}_2$ ($n = 0.017$), further confirming that the HF peak represents the charge transfer process along the material interface.^[28] Overall, according to the DRT approach, information about the role of ex-solved Ag on the electrode surface is discussed.

Furthermore, we utilized electrical conductivity relaxation (ECR) technique to study the surface properties. Indeed, surface exchange rate is one of the key factors affecting the ORR kinetics, thus extraction of the values can further guide the understanding to the function of Ag nanocatalysts. To perform, we first deposited a dense PLD layer of BACNT cathode on Al_2O_3 substrate (BACNT sample). Thereafter, the sample is treated under 4% H_2/Ar at 300 °C to ex-solve Ag nanoparticles (e-BACNT sample), and a subsequent electrical conductivity relaxation (ECR) was performed between $p\text{O}_2 = 0.21\text{--}1$ atm at 550 °C. Finally, by fitting the conductivity curves, we find the surface exchange coefficient (k_{chem}) values (Figure S17, Supporting Information). It is worth noting that after Ag ex-solution, the k_{chem} values shows significant increases (nearly doubled after ex-solution: from 1.46×10^{-5} to 2.67×10^{-5} cm s^{-1}), indicating that Ag ex-solution indeed enhanced the oxygen surface exchange kinetics.

The electrode polarization resistance levels of e-BACN, e-BACT, and e-BACNT are also shown in Figure 3f with those of other benchmark cathodes in order to measure their performance capabilities. The developed material system demonstrates much better electrochemical performance than those of the Sr-containing cathodes, in this case $\text{Ba}_{0.5}\text{Sr}_{0.5}\text{Co}_{0.8}\text{Fe}_{0.2}\text{O}_{3-\delta}$ (BSCF) or $\text{La}_{0.6}\text{Sr}_{0.4}\text{Co}_{0.2}\text{Fe}_{0.8}\text{O}_{3-\delta}$ (LSCF).^[12,37] The performance of the Ag ex-solved BCO cathodes (e.g., e-BACNT: $\approx 0.042 \Omega \text{ cm}^2$ at 600 °C) also exceeds the values reported with layered perovskites such as $\text{PrBa}_{0.5}\text{Sr}_{0.5}\text{Co}_{1.5}\text{Fe}_{0.5}\text{O}_{5+\delta}$ (PBSCF, $\approx 0.056 \Omega \text{ cm}^2$ at 600 °C) and $\text{NdBa}_{1-x}\text{Ca}_x\text{Co}_2\text{O}_{5+\delta}$ (NBCC, $\approx 0.066 \Omega \text{ cm}^2$ at 600 °C) as well as some nanostructured cathodes such as multiphase- $\text{PrBa}_{0.8}\text{Ca}_{0.2}\text{Co}_2\text{O}_{5+\delta}$ -coated LSCF (MP-PBCC-LSCF).^[28,38]

One concern about perovskites containing high levels of Ba is their chemical durability given the high basic nature of Ba ions. Particularly, low tolerance to CO_2 -containing atmospheres is often pointed out, which may critically affect the structure of Ba-containing perovskites.^[15,39] Despite this concern, the Ba-containing host oxide (BCNT) seems to be successfully stabilized with co-doping of Nb and Ta (Figure S18, Supporting Information), and the e-BACNT cathode exhibits much higher tolerance toward poisoning than the BSCF cathode in CO_2 -containing moist air (3 vol% $\text{H}_2\text{O}/\text{air}$), proving its feasibility for practical operations (Figure S19, Supporting Information). In addition, the cathodes tested here show remarkably low activation energies (e.g., e-BACNT: 1.03 eV), meaning they are ideally suited for low-to-intermediate temperature operations.

2.3. Demonstration with Button Cells

The outstanding performance of the e-BACNT cathode is also evaluated in button cells under realistic SOFC operating conditions. First, a typical configuration of an anode support (Ni-SDC|SDC) is prepared. Next, in the button cell design, we also introduce the advanced processing technique of pulsed laser deposition (PLD) in an effort to consolidate the interface contact between the electrode and the electrolyte. The poor electrode-electrolyte contact has been addressed in protonic conducting fuel cells (PCFCs), and to overcome this obstacle, Choi et al. applied a PLD cathode layer at the porous cathode-electrolyte interface.^[40] A striking performance improvement (>30%) was realized by means of a cathode conformal coating in the PCFC. Therefore, it will be interesting to find whether the aforementioned strategy can be extended to SOFCs as well. Accordingly, we similarly incorporate a cathode thin film between the e-BACNT porous cathode and the SDC electrolyte

(hereafter PLD: O cell, Figure 4b,c and Figure S20b, Supporting Information) and compared the performance to that of a conventionally fabricated cell (hereafter PLD: X cell, Figure 4a and Figure S20a, Supporting Information).

The typical polarization curves are recorded by blowing humidified H₂ onto the anode and synthetic air onto the cathode. Still with the conventional button cell configurations (Ni-SDC|SDC|e-BACNT, PLD: X), superior activity of the e-BACNT cathode is attained, with a peak power density of $\approx 1.07 \text{ W cm}^{-2}$ at 650 °C (Figure S21a, Supporting Information). When an extra PLD layer is added, however, the power output of the single cell is only marginally enhanced (Ni-SDC|SDC|PLD-BCNT|e-BACNT, PLD: O). Hence, peak power density of $\approx 1.12 \text{ W cm}^{-2}$ is achieved at 650 °C ($\approx 4.7\%$ increase).

It is noteworthy that the polarization behavior of the SOFCs (Figure 4d,e) with the addition of the cathode interlayer is quite distinct from that of PCFCs. For a more in-depth explanation of this, impedance spectroscopy is conducted at the open-circuit

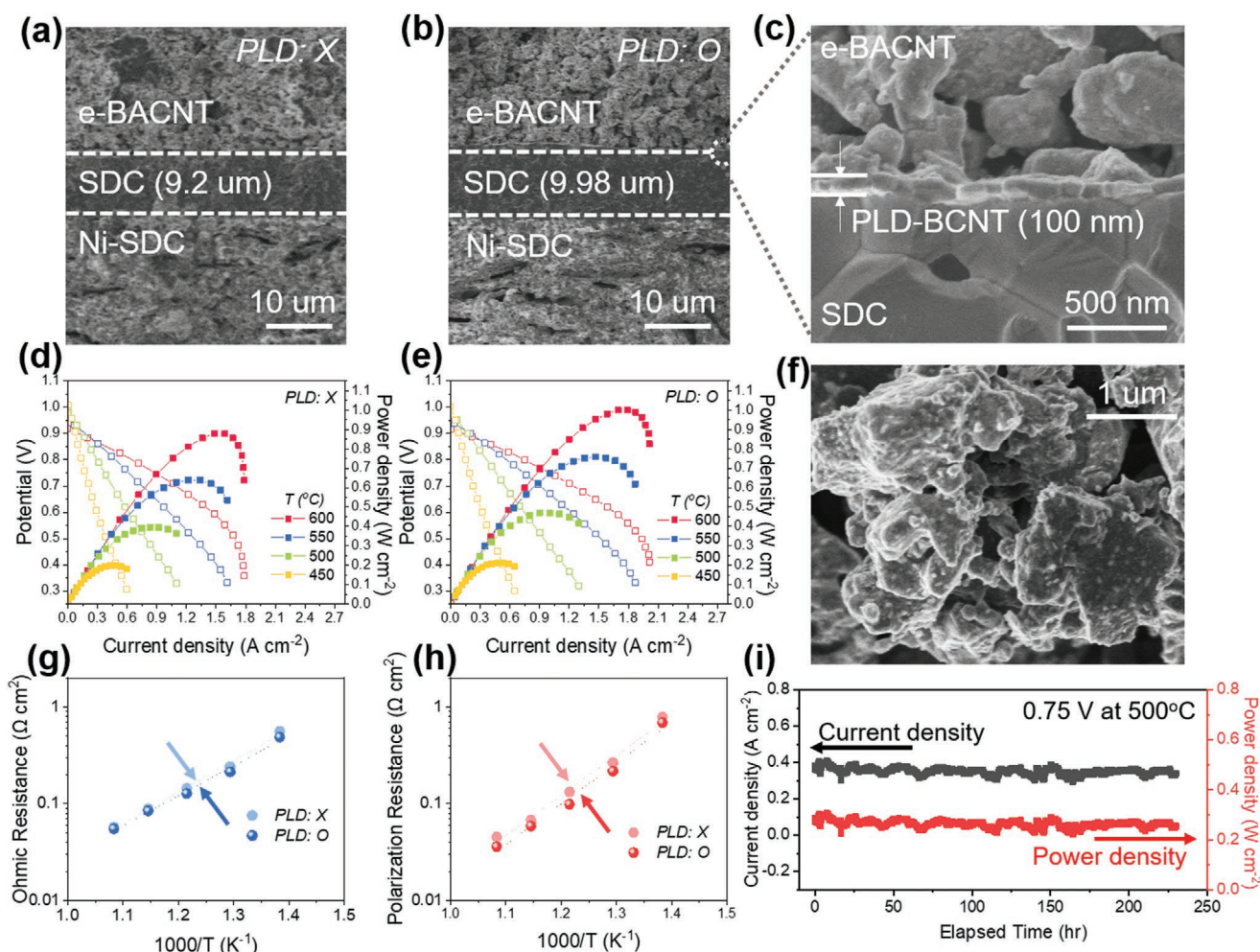


Figure 4. Performance demonstration with button cells: Cross-sectional SEM images of button cells of a) conventional configurations (Ni-Sm_{0.2}Ce_{0.8}O_{2-δ} (SDC)|SDC|Ag ex-solved Ba_{0.95}Ag_{0.05}Co_{0.8}Nb_{0.1}Ta_{0.1}O_{3-δ} (e-BACNT), PLD: X cell), and b) with extra pulsed layer deposition (PLD)-cathode (Ni-SDC|SDC|PLD-BaCo_{0.8}Nb_{0.1}Ta_{0.1}O_{3-δ} (BCNT)|e-BACNT, PLD: O cell). c) Magnified SEM image describing the PLD cathode interlayer, Polarization and power density curves of d) PLD: X cell, and e) PLD: O cell. f) Surface morphology of the e-BACNT cathode after >225 h of operation. g) Corresponding ohmic resistance and h) polarization resistance of single cells, and i) long-term stability data measured with PLD: O cell with a constant voltage load of 0.75 V at 500 °C.

voltage (Figure 4g,h, and Figure S21b, Supporting Information). Accordingly, it was found that the cathode interlayer causes only a trivial advancement in the offset resistance of the button cell. To discuss, for a proton-conducting material, the resistances of the proton transfer along the grain boundaries are notoriously high due to the charge inversion.^[41] Therefore, providing a cathode dense layer over the electrolyte may largely overcome the ion transport (H^+) barrier at the interface. However, it has been suggested that the grain boundary does not critically affect the ionic conductivities in major oxygen anion (O^{2-}) conductors.^[42] Thus, the combination of a cathode PLD layer and a SOFC may not be as effective a strategy as it was in the PCFCs. From a technical standpoint, this implies that the contact between the e-BACNT cathode and the electrolyte interface is sound with good ionic conductive nature; thereby, a high-performance fuel cell can be realized without the requirement of the complex vacuum processing technique.

Nonetheless, the PLD: O cell performs impressively at relatively low temperatures (e.g., $\approx 1 \text{ W cm}^{-2}$ at 600°C , Figure 4e) and operates for more than $\approx 225 \text{ h}$ without a notable degradation, providing evidence of the exceptional stability of the e-BACNT material (Figure 4i). After operation, the e-BACNT cathode surface was characterized with SEM to determine whether the Ag nanoparticles maintained their morphologies. Although some of the particle sizes of Ag were found to be slightly larger compared to the as-synthesized case, the overall particle size was well preserved and remained in the nano domain. Overall, we demonstrate that the newly developed e-BACNT cathode qualifies as a reliable constituent for use in practical SOFC applications.

3. Conclusion

In summary, by integrating Ag nanocatalysts into a highly active $\text{Ba}_{0.95}\text{Co}_{0.8}\text{Nb}_{0.1}\text{Ta}_{0.1}\text{O}_{3-\delta}$ perovskite, a SOFC cathode capable of excellent performance has been demonstrated, achieving very low cathode ASR values of ≈ 0.02 and $0.098 \text{ } \Omega \text{ cm}^2$ at 650 and 550°C , respectively, in a symmetric cell configuration. By utilizing the ex-solution process as a central strategy, firmly anchored Ag nanoparticles notably lower the polarization losses of freshly designed niobium- and/or tantalum-doped BCO perovskites. The superior ORR activity is attributed to the synergistic effect of socketed Ag, which acts as a catalytic core to boost surface exchange rates, combined with the promotion of the charge transfer reaction at the Ag-oxide interface. Accordingly, ex-solution phenomena reshape the landscape of the oxygen reduction reaction occurring on the oxide, thus enhancing the performance. The effective tactics incorporated in this study establish a milestone on the road toward exceptional performance of SOFC cathodes at low-to-intermediate temperature regimes due to the orchestration of the “parent scaffold-offspring metal catalyst” as a key skeleton.

4. Experimental Section

<i>Material</i>	<i>Fabrication:</i>	BCN	$(\text{BaCo}_{0.9}\text{Nb}_{0.1}\text{O}_{3-\delta})$,	BACN
$(\text{Ba}_{0.95}\text{Ag}_{0.05}\text{Co}_{0.9}\text{Nb}_{0.1}\text{O}_{3-\delta})$,	BCT		$(\text{BaCo}_{0.9}\text{Ta}_{0.1}\text{O}_{3-\delta})$,	BACT

$(\text{Ba}_{0.95}\text{Ag}_{0.05}\text{Co}_{0.9}\text{Ta}_{0.1}\text{O}_{3-\delta})$, BCNT $(\text{BaCo}_{0.8}\text{Nb}_{0.1}\text{Ta}_{0.1}\text{O}_{3-\delta})$, and BACNT $(\text{Ba}_{0.95}\text{Ag}_{0.05}\text{Co}_{0.8}\text{Nb}_{0.1}\text{Ta}_{0.1}\text{O}_{3-\delta})$ powders were synthesized by a conventional solid-state reaction method. Stoichiometric amounts of high-purity barium carbonate (BaCO_3 , Alfa Aesar), cobalt oxide (Co_3O_4 , Sigma Aldrich), niobium oxide (Nb_2O_5 , Sigma Aldrich), tantalum oxide (Ta_2O_5 , Sigma Aldrich), and silver nitrate (AgNO_3 , Sigma Aldrich) were mixed and ball-milled using ethanol as solvent media at 400 rpm for 12 h . After ball-milling, the respective powders were dried in an oven and subsequently pelletized into discs. The discs were then calcined at 1150°C for 10 h in ambient air. The resulting discs were subsequently crushed with agar mortar and the above steps (ball-milling, pelletizing and calcination) were repeated to obtain a pure phase.

Fabrication of Symmetric Cells and Single Cells: Symmetric cells with the electrode|SDC|electrode configuration were fabricated to measure the cathode area-specific resistance. SDC powders were purchased from Fuelcellmaterials, Inc. The SDC electrolyte samples were prepared by the dry pressing of the SDC powder, followed by sintering at 1450°C for 5 h in ambient air. The cathode powders were weighed and mixed with an ink vehicle (Fuelcellmaterials, Inc.) at a 1:1 ratio. The resulting colloidal suspension was then ball-milled with ethanol media for 12 h . The excess ethanol was later vaporized in an oven at 90°C . Prepared cathode slurries were then applied onto both sides of the SDC electrolyte by screen-printing and were then fired at 900°C for 2 h under ambient air. To ex-solve the Ag nanoparticles, the electrode was subsequently reduced in $4\% \text{ H}_2/\text{Ar}$ at 300°C . Silver paste was then deposited as the current collector.

An anode-supported cell with the Ni-SDC|SDC|e-BACNT configuration was devised to demonstrate the single cell performance. The anode support was initially prepared by ball-milling NiO, SDC, and starch at a 6:4:1 ratio in ethanol media. After the complete evaporation of ethanol in a drying oven, the anode composite was dry-pressed with a square-steel die $1.3 \times 1.3 \text{ cm}$ in size. Thereafter, the anode-support was fired at 950°C for 1 h in air.

The SDC electrolyte is applied by a drop-coating method. An electrolyte suspension of SDC in an organic binder (mixture of polyvinylpyrrolidone (PVP, Alfa Aesar), butyl benzyl phthalate (Alfa Aesar), triethanolamine (Alfa Aesar), and terpineol (Alfa Aesar)) was drop-coated and subsequently sintered at 1400°C for 5 h . Thereafter, the cathode underwent an identical process for the preparation of symmetric cells.

Cathode Layer Fabrication with the Pulsed Laser Deposition (PLD) Technique: With a cylindrical die, the previously synthesized BCNT powders were pelletized into discs under uniaxial compression. Subsequently, the green body was sintered at 1150°C for 10 h to bake a PLD target.

A dense BCNT thin film was then deposited onto the electrolyte side of the Ni-SDC|SDC anode half-cell by pulsed laser deposition (PLD). An excimer laser (KrF, Coherent COMP Pro 205) with a wavelength of 248 nm , an average energy of $280 \text{ mJ pulse}^{-1}$, and a laser repetition frequency of 5 Hz was used. The substrate was maintained at 650°C with a working pressure of 10 mTorr by pure oxygen gas during the deposition process. The thickness of the BCNT layer was $\approx 100 \text{ nm}$. After the layer deposition step, the sample was annealed in the same chamber at 650°C under 1 Torr with pure oxygen for 20 min for crystallization of the oxide layer.

Physical Characterizations: The crystal structure of the synthesized powder was analyzed by high-resolution X-ray diffraction (X'pert-PRO MRD). The surface morphologies of the symmetric cells were characterized by SEM (Hitachi S-4800). A TEM analysis (Talos F200X) was conducted to verify the phase of the ex-solved nanoparticles. H_2 -temperature-programmed reduction (TPR) was also done to determine the ex-solution condition of the perovskites.

Electrochemical Measurements: Electrochemical impedance spectroscopy (EIS) results of the cathode symmetric cell were obtained by AC impedance measurements using a Biologics VSP-300 device as the workstation (OCV, 1 MHz – 0.01 Hz) in the temperature range of 450 – 650°C . The cells were placed in alumina tube in contact with a pseudo-four-configuration probe with platinum wire. The mixture gases

(O₂-Ar) were flowed into the tube with digital mass flow controllers. The *I*-*V* and *I*-*P* curves were collected using the Biologics VSP-300 device at 0.03 V s⁻¹. An in-lab-constructed fuel-cell testing station operating within the temperature range of 450–650 °C was utilized. During the single cell test, H₂ gas was flowed into the anode side at a flow rate of 75 mL min⁻¹, while 75 mL of synthetic air (N₂: 79%, O₂: 21%) min⁻¹ was fed into the cathode side. DRT analyses were conducted with DRTtools, software obtained from Ciucci's group.^[35]

Supporting Information

Supporting Information is available from the Wiley Online Library or from the author.

Acknowledgements

This work was supported by the Samsung Research Funding Center of Samsung Electronics under Project Number SRFC-MA1502-52.

Conflict of Interest

The authors declare no conflict of interest.

Keywords

Ag, BaCoO_{3-δ}, ex-solution, oxygen reduction reaction, solid oxide fuel cells

Received: February 11, 2020

Revised: March 24, 2020

Published online:

- [1] a) Y. Choi, S. K. Cha, H. Ha, S. Lee, H. K. Seo, J. Y. Lee, H. Y. Kim, S. O. Kim, W. Jung, *Nat. Nanotechnol.* **2019**, *14*, 245; b) T. Li, O. Kasian, S. Cherevko, S. Zhang, S. Geiger, C. Scheu, P. Felfer, D. Raabe, B. Gault, K. J. J. Mayrhofer, *Nat. Catal.* **2018**, *1*, 300.
- [2] D. Neagu, T.-S. Oh, D. N. Miller, H. Ménard, S. M. Bukhari, S. R. Gamble, R. J. Gorte, J. M. Vohs, J. T. Irvine, *Nat. Commun.* **2015**, *6*, 8120.
- [3] D. Neagu, G. Tsekouras, D. N. Miller, H. Ménard, J. T. S. Irvine, *Nat. Chem.* **2013**, *5*, 916.
- [4] C. Duan, R. J. Kee, H. Zhu, C. Karakaya, Y. Chen, S. Ricote, A. Jarry, E. J. Crumlin, D. Hook, R. Braun, N. P. Sullivan, R. O'Hayre, *Nature* **2018**, *557*, 217.
- [5] a) T. Zhu, H. E. Troiani, L. V. Mogni, M. Han, S. A. Barnett, *Joule* **2018**, *2*, 478; b) O. Kwon, S. Sengodan, K. Kim, G. Kim, H. Y. Jeong, J. Shin, Y.-W. Ju, J. W. Han, G. Kim, *Nat. Commun.* **2017**, *8*, 15967.
- [6] N. W. Kwak, S. J. Jeong, H. G. Seo, S. Lee, Y. Kim, J. K. Kim, P. Byeon, S.-Y. Chung, W. Jung, *Nat. Commun.* **2018**, *9*, 4829.
- [7] J. Lu, C. Zhu, C. Pan, W. Lin, J. P. Lemmon, F. Chen, C. Li, K. Xie, *Sci. Adv.* **2018**, *4*, eaar5100.
- [8] S. Liu, Q. Liu, J.-L. Luo, *ACS Catal.* **2016**, *6*, 6219.
- [9] Y.-R. Jo, B. Koo, M.-J. Seo, J. K. Kim, S. Lee, K. Kim, J. W. Han, W. Jung, B.-J. Kim, *J. Am. Chem. Soc.* **2019**, *141*, 6690.
- [10] a) H. Tanaka, M. Uenishi, M. Taniguchi, I. Tan, K. Narita, M. Kimura, K. Kaneko, Y. Nishihata, J. i. Mizuki, *Catal. Today* **2006**, *117*, 321; b) S.-H. Cui, J.-H. Li, X.-W. Zhou, G.-Y. Wang, J.-L. Luo, K. T. Chuang, Y. Bai, L.-J. Qiao, *J. Mater. Chem. A* **2013**, *1*, 9689;
- c) Y.-F. Sun, Y.-Q. Zhang, J. Chen, J.-H. Li, Y.-T. Zhu, Y.-M. Zeng, B. S. Amirikhiz, J. Li, B. Hua, J.-L. Luo, *Nano Lett.* **2016**, *16*, 5303.
- [11] M. Radovic, S. Speakman, L. Allard, E. Payzant, E. Lara-Curzio, W. Kriven, J. Lloyd, L. Fegely, N. Orlovskaya, *J. Power Sources* **2008**, *184*, 77.
- [12] Z. Shao, S. M. Haile, *Nature* **2004**, *431*, 170.
- [13] Y. Chen, S. Yoo, W. Zhang, J. H. Kim, Y. Zhou, K. Pei, N. Kane, B. Zhao, R. Murphy, Y. Choi, M. Liu, *ACS Catal.* **2019**, *9*, 7137.
- [14] Y. Chen, S. Yoo, Y. Choi, J. H. Kim, Y. Ding, K. Pei, R. Murphy, Y. Zhang, B. Zhao, W. Zhang, H. Chen, Y. Chen, W. Yuan, C. Yang, M. Liu, *Energy Environ. Sci.* **2018**, *11*, 2458.
- [15] Y. Zhu, W. Zhou, R. Ran, Y. Chen, Z. Shao, M. Liu, *Nano Lett.* **2016**, *16*, 512.
- [16] a) J. Vieten, B. Bulfin, P. Huck, M. Horton, D. Guban, L. Zhu, Y. Lu, K. A. Persson, M. Roeb, C. Sattler, *Energy Environ. Sci.* **2019**, *12*, 1369; b) L. Sis, G. Wirtz, S. Sorenson, *J. Appl. Phys.* **1973**, *44*, 5553.
- [17] Y. Zhang, R. Knibbe, J. Sunarso, Y. Zhong, W. Zhou, Z. Shao, Z. Zhu, *Adv. Mater.* **2017**, *29*, 1700132.
- [18] W. Zhou, W. Jin, Z. Zhu, Z. Shao, *Int. J. Hydrogen Energy* **2010**, *35*, 1356.
- [19] W. Zhou, Z. Shao, R. Ran, R. Cai, *Electrochem. Commun.* **2008**, *10*, 1647.
- [20] V. Cascos, R. Martínez-Coronado, J. Alonso, *Int. J. Hydrogen Energy* **2014**, *39*, 14349.
- [21] M. Li, W. Zhou, Z. Zhu, *ChemElectroChem* **2015**, *2*, 1331.
- [22] A. Aguadero, C. d. l. Calle, J. Alonso, M. Escudero, M. Fernández-Díaz, L. Daza, *Chem. Mater.* **2007**, *19*, 6437.
- [23] M. Li, W. Zhou, X. Xu, Z. Zhu, *J. Mater. Chem. A* **2013**, *1*, 13632.
- [24] A. Aguadero, D. Pérez-Coll, J. Alonso, S. Skinner, J. Kilner, *Chem. Mater.* **2012**, *24*, 2655.
- [25] W. Zhou, J. Sunarso, M. Zhao, F. Liang, T. Klande, A. Feldhoff, *Angew. Chem., Int. Ed.* **2013**, *52*, 14036.
- [26] M. Li, M. Zhao, F. Li, W. Zhou, V. K. Peterson, X. Xu, Z. Shao, I. Gentile, Z. Zhu, *Nat. Commun.* **2017**, *8*, 13990.
- [27] Z. Shao, M. O. Tadé, in *Intermediate-Temperature Solid Oxide Fuel Cells*, Springer, Berlin, Heidelberg **2016**, p. 247.
- [28] Y. Chen, Y. Choi, S. Yoo, Y. Ding, R. Yan, K. Pei, C. Qu, L. Zhang, I. Chang, B. Zhao, *Joule* **2018**, *2*, 938.
- [29] a) Y. Zhang, A. Zhu, Y. Guo, C. Wang, M. Ni, H. Yu, C. Zhang, Z. Shao, *Appl. Energy* **2019**, *238*, 344; b) P. Zeng, Z. Chen, W. Zhou, H. Gu, Z. Shao, S. Liu, *J. Membr. Sci.* **2007**, *291*, 148.
- [30] J. H. Kim, Z.-Y. Chern, S. Yoo, B. M. deGlee, J.-H. Wang, M. Liu, *ACS Appl. Mater. Interfaces* **2019**, *12*, 2370.
- [31] Y. Chen, Y. Chen, D. Ding, Y. Ding, Y. Choi, L. Zhang, S. Yoo, D. Chen, B. Deglee, H. Xu, *Energy Environ. Sci.* **2017**, *10*, 964.
- [32] a) F. Liang, W. Zhou, Z. Zhu, *ChemElectroChem* **2014**, *1*, 1627; b) W. Zhou, Z. Shao, F. Liang, Z.-G. Chen, Z. Zhu, W. Jin, N. Xu, *J. Mater. Chem.* **2011**, *21*, 15343.
- [33] R. D. Shannon, *Acta Crystallogr. A* **1976**, *32*, 751.
- [34] a) M. Yashima, S. Matsuyama, R. Sano, M. Itoh, K. Tsuda, D. Fu, *Chem. Mater.* **2011**, *23*, 1643; b) U. Farid, H. U. Khan, M. Avdeev, S. Injac, B. J. Kennedy, *J. Solid State Chem.* **2018**, *258*, 859.
- [35] a) M. Saccoccio, T. H. Wan, C. Chen, F. Ciucci, *Electrochim. Acta* **2014**, *147*, 470; b) F. Ciucci, C. Chen, *Electrochim. Acta* **2015**, *167*, 439; c) T. H. Wan, M. Saccoccio, C. Chen, F. Ciucci, *Electrochim. Acta* **2015**, *184*, 483.
- [36] a) A. Leonide, V. Sonn, A. Weber, E. Ivers-Tiffée, *J. Electrochem. Soc.* **2008**, *155*, B36; b) A. Leonide, B. Rüger, A. Weber, W. Meulenber, E. Ivers-Tiffée, *J. Electrochem. Soc.* **2010**, *157*, B234.
- [37] Y. Chen, S. Yoo, Y. Choi, J. H. Kim, Y. Ding, K. Pei, R. Murphy, Y. Zhang, B. Zhao, W. Zhang, *Energy Environ. Sci.* **2018**, *11*, 2458.

- [38] a) S. Choi, S. Yoo, J. Kim, S. Park, A. Jun, S. Sengodan, J. Kim, J. Shin, H. Y. Jeong, Y. Choi, *Sci. Rep.* **2013**, *3*, 2426; b) S. Yoo, A. Jun, Y. W. Ju, D. Odkhuu, J. Hyodo, H. Y. Jeong, N. Park, J. Shin, T. Ishihara, G. Kim, *Angew. Chem., Int. Ed.* **2014**, *53*, 13064.
- [39] C. Duan, D. Hook, Y. Chen, J. Tong, R. J. E. O'Hayre, *Energy Environ. Sci.* **2017**, *10*, 176.
- [40] S. Choi, C. J. Kucharczyk, Y. Liang, X. Zhang, I. Takeuchi, H.-I. Ji, S. M. Haile, *Nat. Energy* **2018**, *3*, 202.
- [41] a) T. Bondevik, H. Ness, C. Bazioti, T. Norby, O. M. Løvvik, C. T. Koch, Ø. Prytz, *arXiv preprint arXiv:1906.03921* **2019**; b) S. Ø. Stub, E. Vøllestad, T. Norby, *J. Mater. Chem. A* **2018**, *6*, 8265.
- [42] S. J. Jeong, N. W. Kwak, P. Byeon, S.-Y. Chung, W. Jung, *ACS Appl. Mater. Interfaces* **2018**, *10*, 6269.